



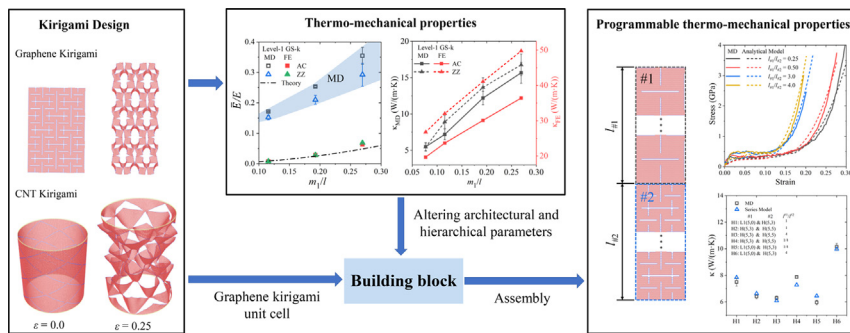
Hierarchical kirigami-inspired graphene and carbon nanotube metamaterials: Tunability of thermo-mechanic properties

Jun Cai^a, Abdolhamid Akbarzadeh^{a,b,*}^a Department of Bioresource Engineering, McGill University, Montreal, QC H9X 3V9, Canada^b Department of Mechanical Engineering, McGill University, Montreal, QC H3A 0C3, Canada

HIGHLIGHTS

- Multiscale simulation and experimentation of hierarchical kirigami metamaterials.
- Tunable thermo-mechanical properties of graphene and CNT kirigami metamaterials.
- Programming the thermo-mechanical properties of nano-architected materials.
- Developing analytical models for the design of heterogeneous nanoscale kirigami.

GRAPHICAL ABSTRACT



ARTICLE INFO

Article history:

Received 21 February 2021

Revised 3 May 2021

Accepted 6 May 2021

Available online 10 May 2021

Keywords:

Kirigami
Hierarchical metamaterials
Graphene
Carbon nanotube
Programmable thermo-mechanical properties

ABSTRACT

Tuning and programming the multiphysical properties of advanced materials are of critical importance for developing the next generation of adaptable multifunctional metamaterials. This study demonstrates the tunability of thermo-mechanical properties of graphene sheets and carbon nanotubes by inspiring from hierarchical kirigami mechanical metamaterials. The theoretical investigation, multiscale simulation, and experimentation show that the thermo-mechanical properties of nano-architected kirigami metamaterials can be tuned by altering geometrical parameters and introducing the hierarchical cutting patterns. Additionally, the thermal conductivity of kirigami-inspired graphene and carbon nanotube metamaterials can be regulated by an external mechanical tension. We develop closed-form formulations for predicting the mechanical behavior of kirigami graphene sheets and carbon nanotubes. Molecular dynamics and finite element simulations are conducted to evaluate theoretical predictions. By analyzing and comparing the results from atomistic and continuum-based simulations, the effect of length scale on the thermo-mechanical properties is explored. We realize that the stress-strain response, thermal conductivity, and buckling-induced 3D patterns of nano-architected graphenes can be programmed by utilizing kirigami building blocks, nano-architectural hierarchy, and heterogeneous material design.

© 2021 The Authors. Published by Elsevier Ltd. This is an open access article under the CC BY-NC-ND license (<http://creativecommons.org/licenses/by-nc-nd/4.0/>).

1. Introduction

Graphene and Carbon nanotube (CNT), typical members of allotropes of carbon, have been considered as promising candidates for a wide variety of applications as nanosensors, nanoresonators, and nanoelectronics owing to their interesting thermo-electro-mechanical properties [1–4]. Nevertheless, some of graphene's

* Corresponding author at: Department of Bioresource Engineering, McGill University, Montreal, QC H9X 3V9, Canada.

E-mail address: hamid.akbarzadeh@mcgill.ca (A. Akbarzadeh).

and CNT's intrinsic properties can hamper their applications. For example, the stretchability of graphene and CNT is limited because of their brittle failure mechanism [2,5]. For applications in the flexible and wearable nanoelectronics, nanomaterials are required to demonstrate a ductile response and retain the device functionalities under high mechanical strains. Furthermore, the tunability and programmability of nanomaterials are two crucial factors for extending the properties of graphenes and CNTs to match the thermo-mechanical requirements of targeted applications of nanomaterials [6,7]. Many strategies have been proposed to address the aforementioned shortcomings. By introducing rationally-designed architectures as the constitutive unit cell, reconfigurable architected materials and structures can be developed in multiple scales. Among various types of architected metamaterials, Kirigami ('kiru' means cut and 'kami' means paper) [8] and Origami ('ori' means fold) [8] have attracted the attention of researchers as a material design strategy to realize the programmability of material/structural properties and to enhance their stretchability across a wide range of length scales [8–12]. Kirigami and origami are, respectively, an old Chinese and Japanese art of paper cutting and paper folding that can exploit local elastic instability to induce complex 3D patterns or configurations upon stretching or compression [13–17].

Graphene kirigami has been reported to be fabricated by employing photo-lithography techniques [8,18]. Experimental tests on graphene kirigami have exhibited a great enhancement in their stretchability and bending stiffness [18]. Regarding thermal transport, engineered defected graphene has been fabricated to control the heat flow for developing high-performance thermal rectifiers [19]. These advances in fabrication and experimental realization of kirigami and origami metamaterials have consequently raised the attention of engineers and material scientists for further exploration of the multiphysical behavior of this category of advanced materials in multiple length scales. Previous investigations conducted by molecular dynamics (MD) simulation were mainly focused on linear cutting patterns [20,21]. However, recent studies in micro/mesoscale have shown the influence of hierarchical patterns on the functionality and deformation mode of kirigami metamaterials [9,22–26]. Inspired by micro/mesoscale kirigami metamaterials, we conduct a comprehensive study on the property of nano-architected kirigami graphene and CNT and explore the significant influence of scale effects on the thermo-mechanical properties of nano-architected metamaterials. As an example of scale effects, the mechanism of heat transport is distinct in different length scales; the phonon scattering contributes to the thermal conductivity in nanomaterials, while the effect of phonon scattering on the suppression of thermal transport vanishes in the microscale [27,28]. In addition, graphene (nanoscale) shows superior mechanical stiffness, strength and elasticity compared to graphite (micro/mesoscale) [2,29]. The supreme properties of graphene and CNT suggest that they could replace other materials in existing applications [2,30].

To the best of the author's knowledge, tunability and programmability of mechanical and thermal properties of kirigami-inspired graphene and CNT metamaterials with hierarchical cutting patterns have not yet been systematically studied in nanoscale. The tunable mechanical and thermal properties of graphene sheet kirigami (GS-k) and carbon nanotube kirigami (CNT-k) with hierarchical cutting patterns are investigated here via MD and finite element (FE) simulations. We first illustrate the in-depth mechanism of deformation and thermal transport of kirigami nanomaterials. We show that the mechanical instabilities induced out-of-plane deformation as well as the stress-strain response can be tuned by geometrical parameters and the arrangements of cutting patterns. We find that applying an external uniaxial tension enables tuning the thermal conductivity of GS-k and CNT-k. Finally,

we establish closed-form analytical models to predict and program the stress-strain response and heat conduction within a heterogeneous hierarchical GS-k. The macroscopic counterparts of the designed nanoscale metamaterials are also fabricated and tested to approve the nonlinear mechanical response and the process of transforming 2D flat sheets to 3D geometries by conducting mechanical strain experimentally.

2. Methods

2.1. Molecular dynamics simulation

All atomic simulations are conducted using the large-scale atomic molecular massively parallel simulator (LAMMPS) [31]. The Open Visualization Tool (OVITO) [32] is employed to visualize the evolution of atomic structures. AIREBO [33] potential function is used to describe C-C and C-H interatomic interactions. Hydrogen atoms are added to stabilize cuts in GS-k and CNT-k by passivating dangling bonds at the crack boundary [34]. The cutoff distance between C-C is set 2.0 Å [34] to avoid the spurious strengthening effect. The integration time step is set as 0.5 femtoseconds (fs). Periodic boundary conditions are applied to two planner directions, and a free boundary condition is used in the out-of-plane direction in GS-k. The out-of-plane dimension of the simulation box is set to be larger than the thickness of the monolayer graphene to capture the out-of-plane deformation. Energy minimization is first performed by the conjugate gradient algorithm to obtain a stable kirigami nanostructure. For GS-k, all systems are relaxed in the isothermal-isobaric ensemble (NPT) for 25 picoseconds (ps). The samples are then subjected to a homogeneous tensile deformation by rescaling the vertical coordinates of all atoms in the simulation box. In addition, the stress along the transverse direction is controlled by using NPT ensemble to ensure the uniaxial loading condition [27]. The strain rate is set at $1 \times 10^9 \text{ s}^{-1}$. The axial tensile stress is calculated by averaging the virial stress of all atoms in the system. For CNT-k, all systems are relaxed in the canonical ensemble (NVT) for 25 ps. Then the bottom four-layer carbon atoms are frozen, and the top four-layer carbon atoms are given a velocity along the z direction to simulate the uniaxial tensile deformation. The strain rate is set at $1 \times 10^9 \text{ s}^{-1}$. The axial tensile stress is calculated by averaging the virial stress of all free atoms in the system.

The thermal conductivity is obtained by a reverse non-equilibrium MD (rNEMD) method, in which the heat flux is imposed on the system to generate a temperature gradient [20,33]. The system is divided into 50 slabs along the heat flow direction to extract the temperature profile. As shown in Figs. 3 and 4, the heat and sink reservoirs are located at the middle and the end of the kirigami nanostructure, respectively (the carbon atoms at the two ends of CNT-k are fixed). Periodic boundary conditions are applied in the two in-plane directions in GS-k. The initial relaxed configuration is equilibrated at 300 K in an NVT ensemble for 4×10^5 steps with a time step of 0.5 fs. Then the kirigami nanostructure is switched to a micro-canonical ensemble (NVE) to conserve energy. The kinetic energy is swapped between the coldest atoms in the heat sink slabs and the hottest atoms in the heat source in NVE ensemble to induce the heat flux. Then, the heat flux is calculated as:

$$J = \frac{\sum \frac{1}{2}(m\nu_h^2 - m\nu_c^2)}{t_{swap}} \quad (1)$$

where, the t_{swap} is the total time of exchanging kinetic energy, ν_h and ν_c are the velocity of atoms in hot and cold slabs, respectively.

The temperature distribution in the heat flux direction is captured after 1 nanosecond (ns) when the system reached the non-

equilibrium steady state. Then, the final temperature profiles are obtained by averaging the data of the last 4×10^6 time steps (2 ns). As shown in Fig. S10, the temperature gradient is obtained by a linear fitting in the labeled region. Finally, the thermal conductivity is calculated by using the Fourier law as:

$$\kappa = \frac{J}{A \frac{\partial T}{\partial l}} \quad (2)$$

where A is the cross-sectional area of kirigami nanostructures. To compare our MD results with previous research, we assume a thickness of 0.34 nm for all MD samples [20].

2.2. Finite element analysis

Finite Element simulations are conducted using the commercially available ANSYS Workbench 2019 R2 software. The mechanical response of kirigami metamaterials is simulated by employing the explicit Dynamics module. One side of the kirigami graphene and CNT samples are fixed in the loading direction, while a vertical displacement is applied on the opposite side. To trigger the instability, an imperfection is introduced by applying two opposing small forces normal to the sheet plane at the longer edge of each cut during the initial step of the simulation. There is no imperfection introduced to CNT models during the simulation. The thermal transport within the kirigami metamaterial is simulated by employing steady-state thermal module. For thermal analysis, the temperature of one side is kept at 14 °C while the temperature of the opposite side is set as 30 °C. The remaining sides are thermally insulated ($q = 0$). Furthermore, it is noted that the material parameters obtained from MD simulations cannot be directly used in the FE simulation because these parameters contain the thickness effect [35,36]. So, the effective thickness of graphene and CNT should be identified to exclude the thickness effect. The effective thickness used in FE calculation is 1.281 Å (zigzag) and 1.267 Å (armchair) [35].

3. Hierarchical kirigami graphene and CNT designs

The atomic structures and the geometrical parameters of GS-k and CNT-k are depicted in Fig. 1. Level-1 GS-k patterns are com-

posed of mutually orthogonal straight line cuts (blue lines) that divide a square unit cell (building block) into four connected sub-squares with the hinge width m_1 . The hybrid level-2 hierarchical GS-k pattern is constructed by placing orthogonal line cuts into sub-square domains of the level-1 cuts, where the cuts (tawny lines) are rotated by $\pi/2$, to divide each sub-square domain into four squares with the hinge width m_2 (Fig. 1b). A self-similar level-2 hierarchical GS-k pattern can be constructed by repeating the same cuts of level-1 in each sub-square with the hinge width m_2 (Fig. 1c). The designed hinge width of GS-k should follow the limitation: $m_i < l/i$ (i is the hierarchical level, $l = 6.39$ nm for all samples in the main text). The pattern of orthogonal level-1 CNT-k is the same as level-1 GS-k created by folding a flat level-1 perforated graphene sheet into a cylindrical shell (Fig. 1d). The last model, triangular level-1 CNT-k, is constructed by placing triangular cuts with cutting length $2(l-m_1)$ and cutting angle $\pi/3$. From the snapshots of the deformed GS-k and CNT-k shown in Fig. 1, it is found that the mechanical responses of kirigami nanostructures with distinct cutting patterns are remarkably different. The hierarchical graphene sheets can demonstrate more complex surface textures induced by the out-of-plane deformation induced by local buckling. To better understand the mechanical behavior of GS-k and CNT-k, the mechanical properties of GS-k are systematically investigated for alternative chirality (Armchair/Zigzag) and geometrical parameters in Section 4, the stress-strain behavior of CNT-k metamaterials is discussed in Section 6.

4. Tunable mechanical properties of kirigami graphene

The stress-strain curves and deformation contours of a series of GS-k comprised of 2×3 unit cells under a uniaxial tensile load are shown in Supplementary Material S1-S2. It is found that the hierarchical pattern alters the stress-strain response as well as the deformation behavior of GS-k. More specifically, the ratio m_1/m_2 plays a crucial role in the buckling induced 3D patterns in the hierarchical level [9]. As observed from the stress-strain curves (Figs. S2-S4 in Supplementary Material), the FE response of the GS-k is similar to the post-buckling response of kirigami sheets [22]. For the micro/mesoscale level-1 kirigami structures, the initial linear elastic regime corresponds to the in-plane bending of

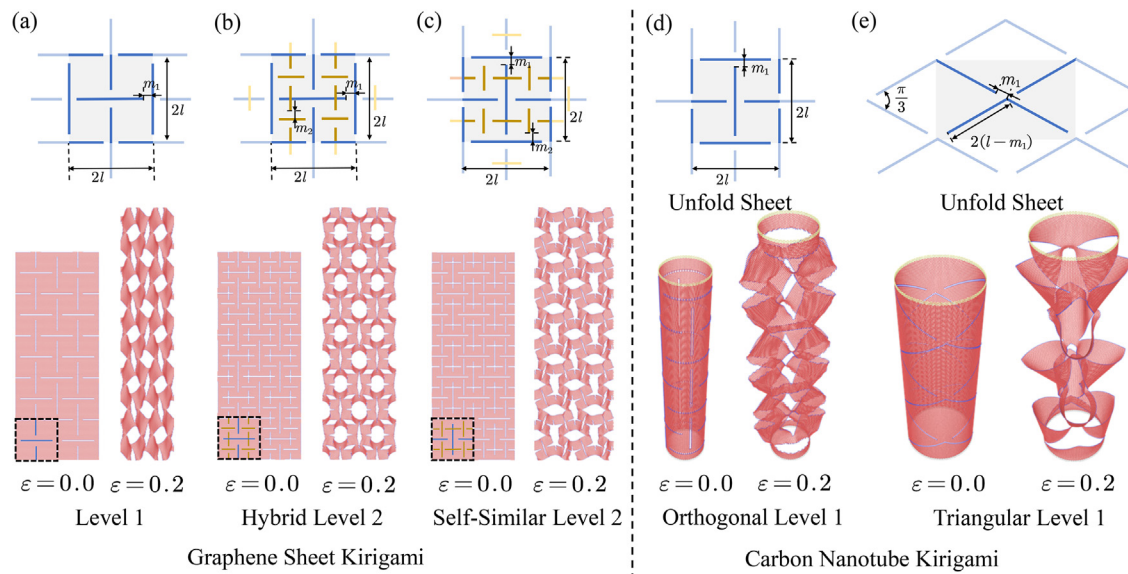


Fig. 1. Schematic kirigami graphene unit cells comprised of an array of orthogonal cuts: (a) level-1 GS-k; (b) level-2 hybrid GS-k; (c) level-2 self-similar GS-k, and their corresponding configuration at certain levels of strain based on MD simulation. Schematic kirigami CNT unit cells (two unit cells form the full perimeter of the cylindrical shell): (d) level-1 CNT-k with orthogonal cuts and (e) level-1 CNT-k with triangular cuts, and corresponding configuration at certain levels of strain based on MD simulation.

hinges governed by the in-plane rotation of the square domains. The effective Young's modulus of level-1 GS-k in microscale can be expressed by $\bar{E} = 2E(m_1/l)^2/3$ [13], where E is the Young's modulus of pristine graphene. Based on the reported theory [9] for mechanical deformation of level-1 kirigami structure with orthogonal cutting patterns, we derive the expression for the Young's modulus of the hierarchical level-2 GS-k as (details can be found in [Supplementary Material S3](#)):

$$\bar{E} = C(m_2, l) \frac{2}{3} \left(\frac{m_1}{l} \right)^2 E \quad (3)$$

where $C(m_2, l)$ is a coefficient function related to the geometry of hierarchical level-2 GS-k.

Upon plotting \bar{E} as a function of m_i/l in [Fig. 2a](#), we find a good agreement between the theoretical predictions and FE results, while MD results show great deviation with theoretical and FE results. Three main factors that result in the deviation between the effective Young's modulus of GS-k in nanoscale (*MD result*) and microscale (*FE and Theoretical results*) are summarized as follows: (1) The surface of GS-k is not flat after relaxation; (2) The thickness of GS-k is overestimated in MD simulation; (3) The size dependency of stress-strain response of GS-k in nanoscale (more details can be found in [Supplementary Material S3](#)). Furthermore, the theoretical results are obtained based on the isotropic material properties that cannot accurately describe the deformation behavior of anisotropic 2D materials. Although the theoretical and FE analyses cannot predict the correct stiffness of GS-k in nanoscale, their results show the same trend as MD's predictions. The stiffness of GS-k can be tuned by adjusting the hinge width; it can be increased dramatically by increasing the ratio (m_i/l) .

In addition to the control of initial stiffness, the kirigami patterns can also tune the yield and failure strains of GS-k ([Fig. 2b](#)).

Each domain rotates around its hinges to produce expandable structures upon stretching. The rotation angle (β in [Fig. S7](#)) determines the final configuration of the stretched GS-k [37]. The number of independent variables (rotation angles) increases by rising the hierarchical level; namely, level-2 GS-k has more degrees of freedom for deformation. The domains keep rotating both in-plane and out-of-plane till a critical strain, named yield strain, is reached. Considering the hinge width, the nominal strains of level-1 GS-k along the loading direction can be determined by:

$$\varepsilon = \frac{\sqrt{(l - m_1)^2 + m_1^2}}{l} (\sin\beta + \cos\beta) - 1 \quad (4)$$

where $0 \leq m_1 < l$. After the yield point, the hinge continues to be stretched with further strain (the tunable yield strain is presented in [Supplementary Material S6](#)). The stress concentration is mainly distributed at the hinges of the cuts. The carbon atoms in graphene are connected by sp^2 bonds [36]. The stress concentration leads to the break of sp^2 bonds at the tip of cuts resulting in the sharp stress decrease at the second peak point ([Fig. S7b](#) in [Supplementary Material](#)). The breaking of the sp^2 bonds results in a decrease of hinge width, which means the domains could continue rotating. This process repeatedly proceeds until the whole sample fails, leading to the zigzag-like stress-strain curves in [Fig. S7b](#). Before the breaking of the last bonds, the level-1 GS-k can be regarded as four domains connected by four sp^2 bonds. Then the hinges can be treated as "free hinges". Moreover, the last bond along the loading direction breaks when the distance between the carbon atoms exceeds the cut-off distance. Then, the failure strain of level-1 GS-k can be determined by substituting $m_1 = 0$ in Eq. (4) as:

$$\varepsilon = (\sin\beta + \cos\beta) - 1 \quad (5)$$

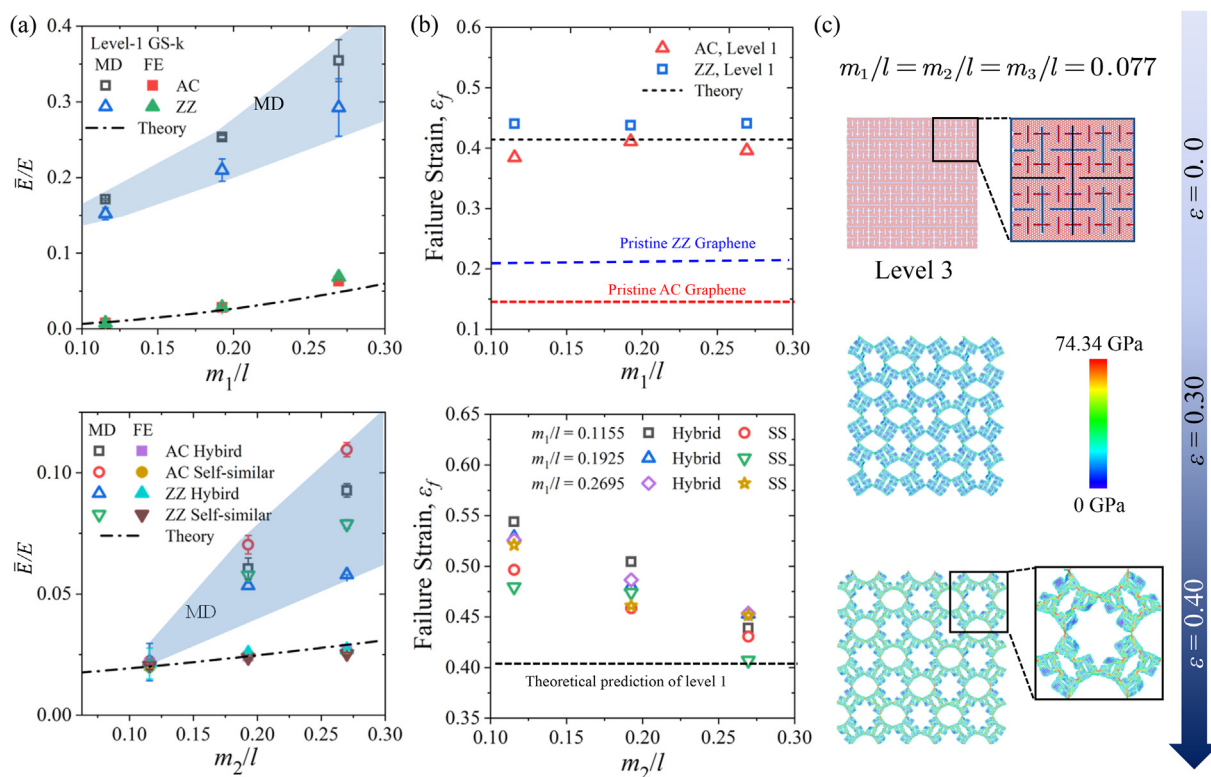


Fig. 2. (a) Normalized effective Young's modulus \bar{E}/E as a function of m_i/l determined by computational simulation and theoretical analysis. (b) Failure strains of level-1 and level-2 unit cells are determined by MD simulation for alternative geometrical ratios (m_i/l). (c) Evolution and reconfiguration of nanostructure in hierarchical GS-k metamaterial with the orthogonal cuts subjected to the biaxial tension; contour displays the von Mises stress.

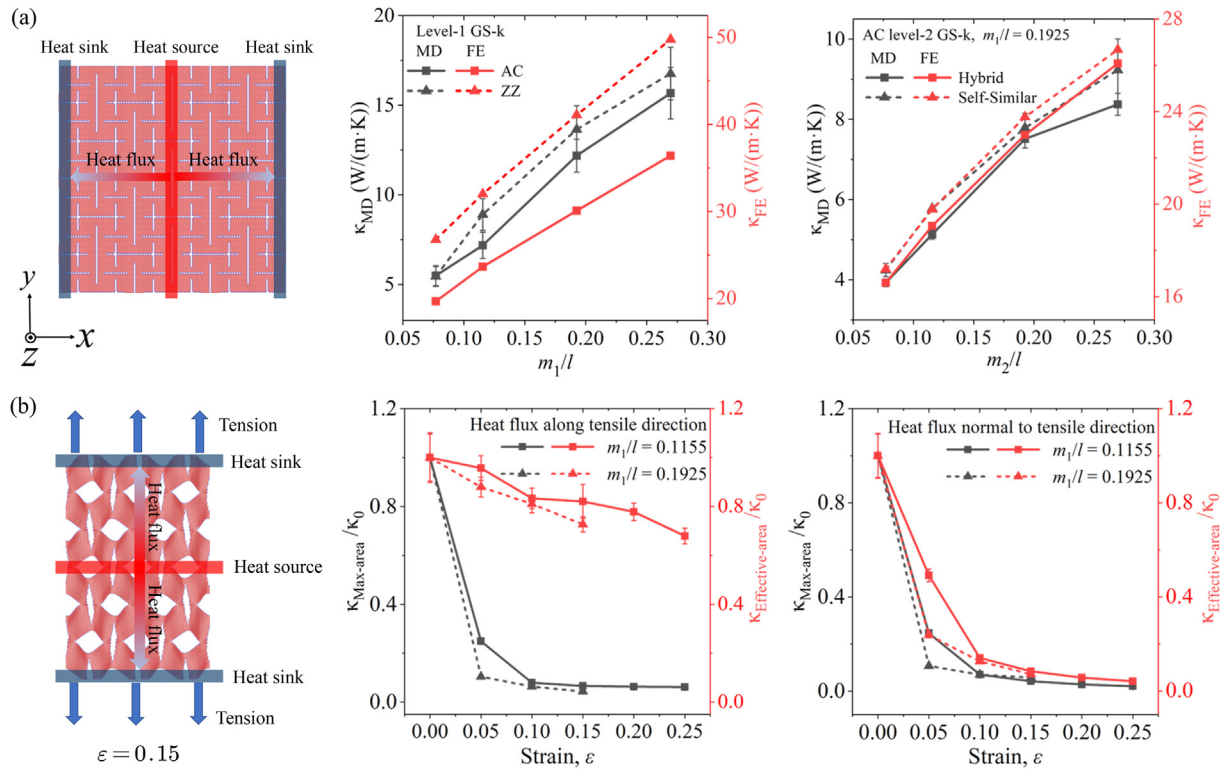


Fig. 3. Thermal transport behavior of GS-k. (a) Thermal conductivity of GS-k as a function of m_i/l determined by MD and FE simulations. (b) Thermal conductivity of level-1 GS-k as a function of uniaxial tensile strain.

where $\beta = 1/4\pi$. As shown in Fig. 2b, the failure strains of level-1 GS-k obtained by MD simulation is consistent with the theoretical prediction. The failure strain of level-1 GS-k is independent of the ratio m_1/l . The degree of freedom increases in hierarchical GS-k [37]. As shown in Fig. S2, the ratio m_1/m_2 plays a crucial role in deformation behavior. The hierarchical cuts (level-2 cuts) are easier to be opened with a smaller hinge width (m_2), leading to the increase of failure strain of hierarchical GS-k (Fig. 2b). However, this positive effect for the failure strain weakens with the increase of hierarchical hinge width (m_2) because the hierarchical cuts are hard to be opened, especially when $m_2 > m_1$.

In addition, the rotation of domains around hinges leads to the lateral expansion of GS-k when subjected to a longitudinal extension resulting in negative Poisson's ratio (more details can be found in Supplementary Material S7) [37]. The one-atomic-thick graphene sheet is flexible, making the GS-k easier to shrink during the tension. Additionally, decreasing the ratio of hinge width and domain's length or increasing the hierarchical level (Fig. S8c in Supplementary Material) weakens the stiffness of hinges and makes the structures more flexible. Therefore, the hinges can no longer hold structure and lead to the collapse of nanostructure when subjected to a uniaxial tensile load. However, the GS-k with level-3 cutting patterns can expand homogeneously in planar directions through the domain rotation around hinges when subjected to biaxial tensile loads (Fig. 2c).

5. Tunable thermal transport of GS-k

In addition to the control of mechanical properties, kirigami nanostructures can tune the thermal transport property of graphene sheets. Fig. 3a depicts the computational modeling of GS-k in MD simulation, where the heat source and sink slabs are located at the middle and at the end of the system. We first study the effect of geometrical parameters on the thermal conductivity of GS-k at

room temperature ($T = 300$ K). For pristine graphene in the absence of tensile strain, the thermal conductivities in the armchair and zigzag directions are around $84 \text{ Wm}^{-1}\text{K}^{-1}$ and $115 \text{ Wm}^{-1}\text{K}^{-1}$, respectively, which are consistent with previously reported results [38]. The thermal conductivity of GS-k with different ratios (m_i/l) determined by MD and FE simulation is shown in Fig. 3a. The error bar is obtained from the linear fitting of the temperature gradient in MD simulation (Fig. S10 in Supplementary Material). The minimum thermal conductivity of GS-k is around $5 \text{ Wm}^{-1}\text{K}^{-1}$ using the present MD simulation. The maximum reduction can be up to 96% for $m_1/l = 0.077$ in level-1 GS-k. The reduction of thermal conductivity can be more severe in hierarchical GS-k. It is also worth to investigate the effect of passivation with hydrogen atoms on the thermal conductivity since the hydrogen atoms are expected to stabilize the cuts in graphene sheets by passivating dangling bonds at the cut boundary (Supplementary Material S10) [34,39]. However, introducing the cutting patterns decreases the thermal conductivity more considerable than the hydrogenous atoms [20]. Since we aim to study the effect of geometrical parameters and mechanical strain on the thermal conductivity of GS-k, the influence of hydrogen termination is neglected in this investigation.

To understand the reduction mechanism of the thermal conductivity for GS-k, temperature profiles of the pristine graphene sheet and GS-k are plotted in Fig. S10 in Supplementary Material. The temperature shows a linear decrease from a hot source to the heat sink in pristine graphene, while discontinuous temperature gaps are observed in GS-k. The hinges between the domains act as an interface that blocks the thermal transport leading to an abrupt temperature decrease (Supplementary Material S11). It is noted that the thermal transport in nanoscale is related to phonons propagation. When phonons attempt to pass through cutting barriers in GS-k, several phonons are scattered. Hence, only a few phonons can pass through the hinges, resulting in increased thermal resistance and decreased phonon transport efficiency [20,27]. In

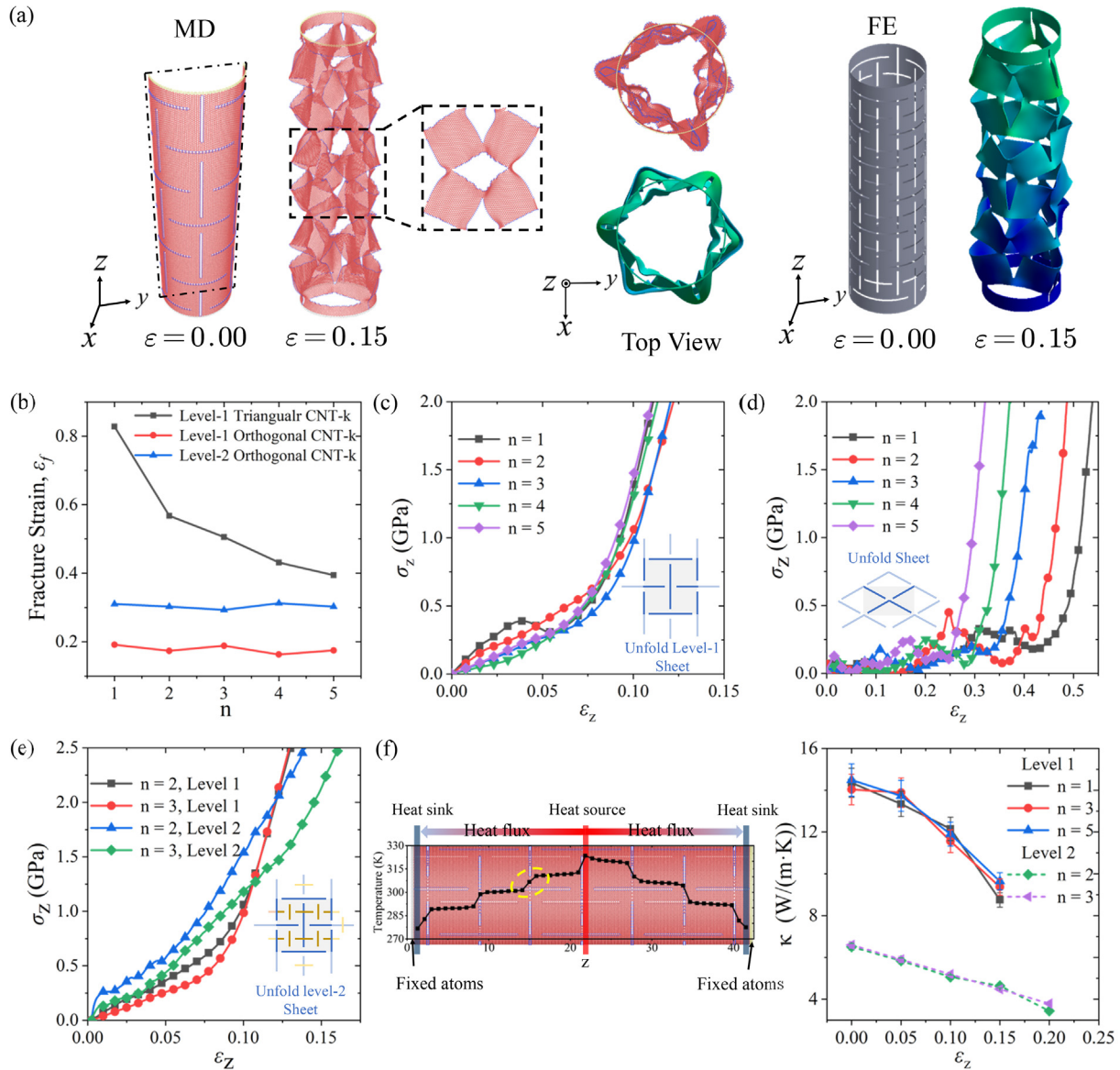


Fig. 4. (a) MD and FE models of CNT-k with orthogonal cuts comprising 3 unit cells along the circumference with $m_1/l = 0.1925$ at different levels of strains. The top view at $\varepsilon = 0.15$ is used to show the pop-up deformation. For simplicity, a half of the symmetric initial MD model is shown. (b) failure strain as a function of n for different patterns and hierarchical levels. (c)-(e) Stress-strain curves of CNT-k. (f) Schematic model for reverse non-equilibrium molecular dynamics simulation of CNT-k with orthogonal patterns, and the corresponding temperature profile; Thermal conductivity of CNT-k as a function of uniaxial strain for different n and hierarchical levels.

Fig. 3a, the MD and FE results show the same trend for thermal conductivity of GS-k with respect to the hinge width ratio. However, the thermal conductivity determined via FE simulation is much larger than the MD results due to the different influenceable factors in nano/microscale [40]. For the atomic-scale system, the mean-free-path of graphene ($\sim 1 \mu\text{m}$) [41] is larger than the length of GS-k, implying that the phonon-cut scattering effect dominates the thermal transport in GS-k [20]. However, the effect of phonon scattering on the suppression of thermal transport vanishes in microscale; as a result, the thermal conductivity in microscale approaches the diffusive heat transfer [27]. From the above analysis, we can conclude that the thermal conductivity of GS-k can be tuned by altering the geometrical ratio, m_1/l , which causes the alteration of the phonon-cut scattering effect. In addition, increasing the hierarchical level of cutting patterns can tailor the thermal conductivity of the graphene sheet. The phonon-cut scattering becomes more pronounced with the increased hierarchy. Hence,

the engineering of cutting patterns can offer an effective paradigm for tuning thermal transport in graphene.

Herein, **Fig. 3b** presents the tunability of the thermal conductivity of level-1 GS-k by applying a mechanical strain (strain dependency of thermal conductivity of hierarchical GS-k is presented in [Supplementary Material S12](#)). For both cases of heat flux along or normal to the tensile strain direction, the thermal conductivity decreases with the increase of applied strain, which is in good agreement with the previous study [20]. The decline of thermal conductivity with tensile strain might be due to the overestimation of the heat flux area [20]. To exclude the effect of overestimated cross-sectional area, two different heat flux areas are considered: (1) *Maximum area*, that is the rectangle area of the cross section where the width is the sample width and the thickness is the maximum thickness of the out-of-plane deformation; (2) *Effective area*, that is defined as the length of the cells normal to the heat flux direction times the thickness of graphene $t = 0.34 \text{ nm}$. The thermal conductivity of GS-k decreases with the increased strain in both

cases. The buckling-induced out-of-plane deformation is activated and enhanced with an increase of strain, which enhances the interface phonon scattering that weakens the ability of thermal transport [38]. We explore tuning the thermal conductivity of graphene by altering the cutting patterns. More details have been presented in [Supplementary Material S13](#).

6. Kirigami CNT

After investigating the mechanical behavior and thermal transport in kirigami nano-sheets (graphene), we now focus on their cylindrical counterparts: kirigami nano-shells (CNT). The CNT-k comprises an array of $n \times 3$ unit cells where the n denotes the number of unit cells along the circumference of the cylinder ($n = 1, \dots, 5$). In [Fig. 4a](#), we show snapshots of CNT-k at different levels of applied tensile strain analyzed by MD and FE simulation. In the CNT-k with orthogonal cutting patterns, both the MD and FE exhibit similar deformation behavior. All the square features pop up simultaneously, forming a uniform 3D textured surface that becomes more accentuated with the increase of strain ([Fig. 4a](#) and Movie S1, see more details in [Supplementary Material S14](#)). One selected unit cell is zoomed in to gain an insight into the physics behind the mechanical behavior. The domains rotate around the hinges, similar to the deformation mechanism of GS-k. Nevertheless, suffering from the fixed boundaries at the top and the bottom of the CNT-k sample, the hinges are stretched and failed before the domains reach the locked points. This observation is fully consistent with the MD results presented in [Fig. 4b](#). Additionally, increasing the hierarchical level is an effective strategy to increase the failure strain of CNT-k.

Next, we explore the possibility of tuning mechanical behavior via placing triangular cuts [22,42] and increasing the hierarchical

level, as shown in [Fig. 4c–e](#). The details of geometrical parameters have been illustrated in [Fig. 1](#). In the CNT-k with orthogonal cuts, the stress-strain response seems independent on the unit cell's curvature. By contrast, the plateau stress regime of the CNT-k with triangular cuts increases with the decrease of n . Similar phenomena can be observed in [Fig. 4b](#); the failure strain of CNT-k with triangular cuts decreases with the increased value of n ; however, the value of n does not affect the stretchability of CNT-k with orthogonal cuts. In CNT-k with triangular cuts, the hinges in the same layer (perpendicular to the loading direction) break simultaneously when the strain reaches a critical value defined as failure strain (Movie S2). However, in CNT-k with orthogonal cuts, the hinges break in sequence (Movie S1). Namely, the CNT-k with orthogonal cuts keeps being deformed after the first failure of a hinge, indicating that the kirigami nanostructure obtains extra freedom to support further deformation. To compare the failure strain between these two designed cutting patterns, we consider the strain at which the first break of hinges occurs as the failure strain. Notably, the characteristics of the pop-up phenomena and the mechanical response of CNT-k can be controlled by carefully selecting the cutting patterns, the curvature of the unit cell, and the hierarchical level.

Finally, we select the CNT-k with orthogonal cuts, the same patterns considered for GS-k, to investigate the thermal transport ([Fig. 4f](#)). From the temperature gradient of CNT-k (presented in [Fig. 4f](#) for $n = 3$), we find that the temperature gradient in the cut region (circled by a yellow dashed ellipse) is much higher than other parts of CNT-k, indicating a lower local thermal conductivity at these parts and leading to the phonon scattering [20]. Furthermore, the CNT-k reveals a strong strain-dependent thermal conductivity. The thermal conductivity decreases with the increased strain due to the increased interface phonon scattering caused by pop-ups [20,27], softening of phono modes, and the increase of lat-

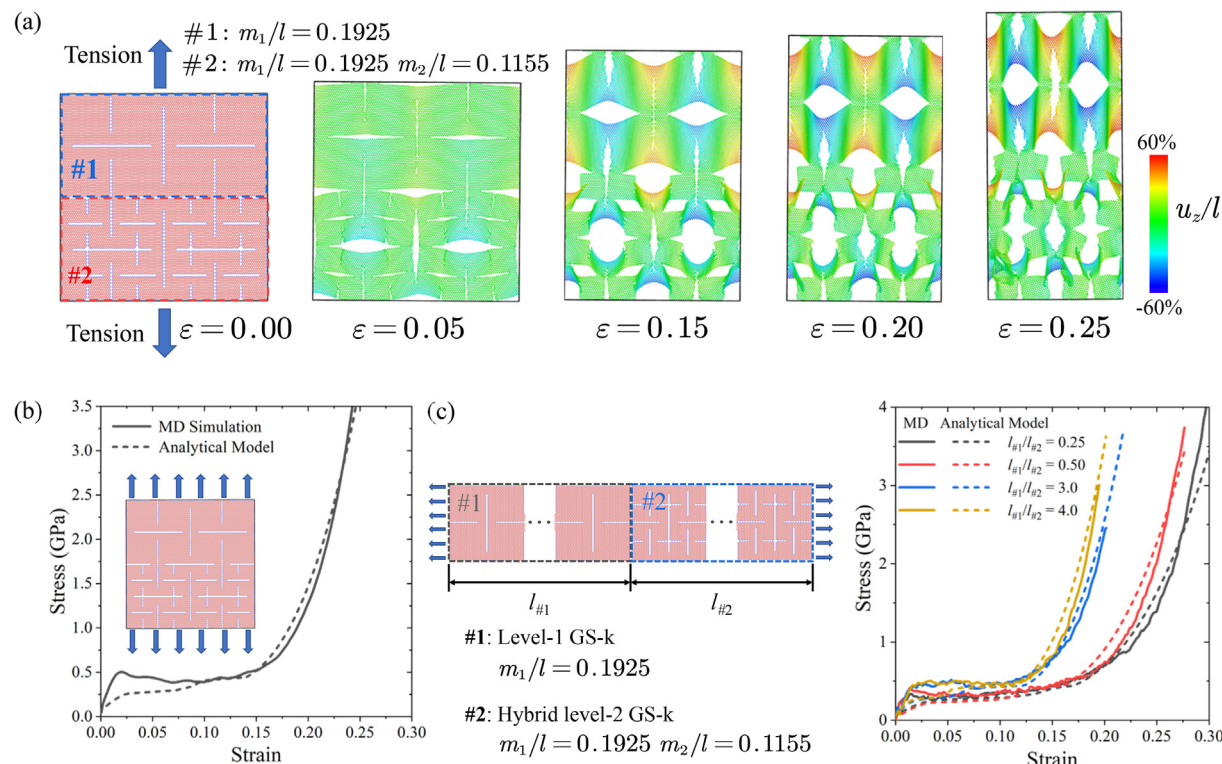


Fig. 5. (a) MD snapshots of the heterogeneous kirigami system with two building blocks connected in series at different levels of applied strains. The contour displays the normalized out-of-plane displacement. (b) Stress-strain response of the combined heterogeneous system as predicted by the analytical model and MD simulation. (c) A schematic heterogeneous GS-k with two building blocks in series characterized by different length $l_{\#1}$ and $l_{\#2}$, and the corresponding stress-strain response predicted by the analytical model and MD simulation.

tice anharmonicity induced by the stretch of hinges [20,43]. The effect of phonon scattering is reinforced by increasing the hierarchical level, resulting in further reduction of thermal conductivity.

7. Programming stress-strain response

After understanding the effect of geometrical parameters, cutting patterns, and architectural hierarchy on the mechanical response of uniform/homogeneous GS-k, we design heterogeneous GS-k and develop theoretical and numerical algorithms to predict their mechanical behavior. We first consider investigating heterogeneous GS-k characterized by kirigami patterns connected in series (subscript “s” presents the series model). When the combined heterogeneous system is subjected to a uniaxial tensile load, the nominal stress is identical in all n building blocks [9], namely

$$\sigma_s = \sigma_{\#i} = \dots = \sigma_{\#n} \quad (6)$$

The total elongation of the system is given by the summation of the elongations of each building block, i.e., the elongation of each building block in-series is independent of the other [44]. Then the strain of the heterogeneous system is given by (See S15 in Supplementary Material):

$$\varepsilon_s = \sum_{i=1}^{i=n} \frac{\varepsilon_{\#i} L_{\#i}}{L_s} \quad (7)$$

where ε_s , σ_s and $L_s = \sum_{i=1}^{i=n} L_{\#i}$ represent the strain, stress, and initial length of the heterogeneous system in the series connection, respectively; $\varepsilon_{\#i}$, $\sigma_{\#i}$ and $L_{\#i}$ represent the strain, stress, and initial length of the i^{th} building block, respectively. Therefore, the stress–

strain response of the heterogeneous system can be simply predicted by using Eqs. (6) and (7) that takes the stress–strain curves obtained for each building block via MD simulation as an input.

Fig. 5a shows a heterogeneous GS-k that is comprised of two different kirigami patterns connected in series (#1: $m_1/l = 0.1925$; #2: $m_1/l = 0.1925$, $m_2/l = 0.1155$). The deformation behavior of each building block in this heterogeneous GS-k subjected to uniaxial tension is similar to the corresponding deformation presented in Fig. S2. As shown in Fig. 5b, the predicted stress–strain curve and the MD simulation of the heterogeneous GS-k demonstrate excellent agreement, indicating that the developed analytical model is viable for predicting the stress–strain behavior of heterogeneous kirigami nanostructures composed of building blocks with known stress–strain relations. Additionally, the stress–strain response of heterogeneous GS-k can be tuned by altering the length ratio of the building blocks ($l_{\#1}/l_{\#2}$) as presented in Fig. 5c.

We also investigate the heterogeneous GS-k characterized by kirigami patterns connected in parallel. The details of theoretical analysis can be found in Supplementary Material S15. The predictions of the stress–strain response of more combined heterogeneous GS-k are presented in Supplementary Material S16. Generally, the aforementioned investigation offers a tool for the rapid engineering of mechanical properties of GS-k to achieve a desired stress–strain response.

8. Programming thermal transport

In addition to the mechanical properties, the thermal transport characteristics of GS-k can be programmable by the heterogeneous

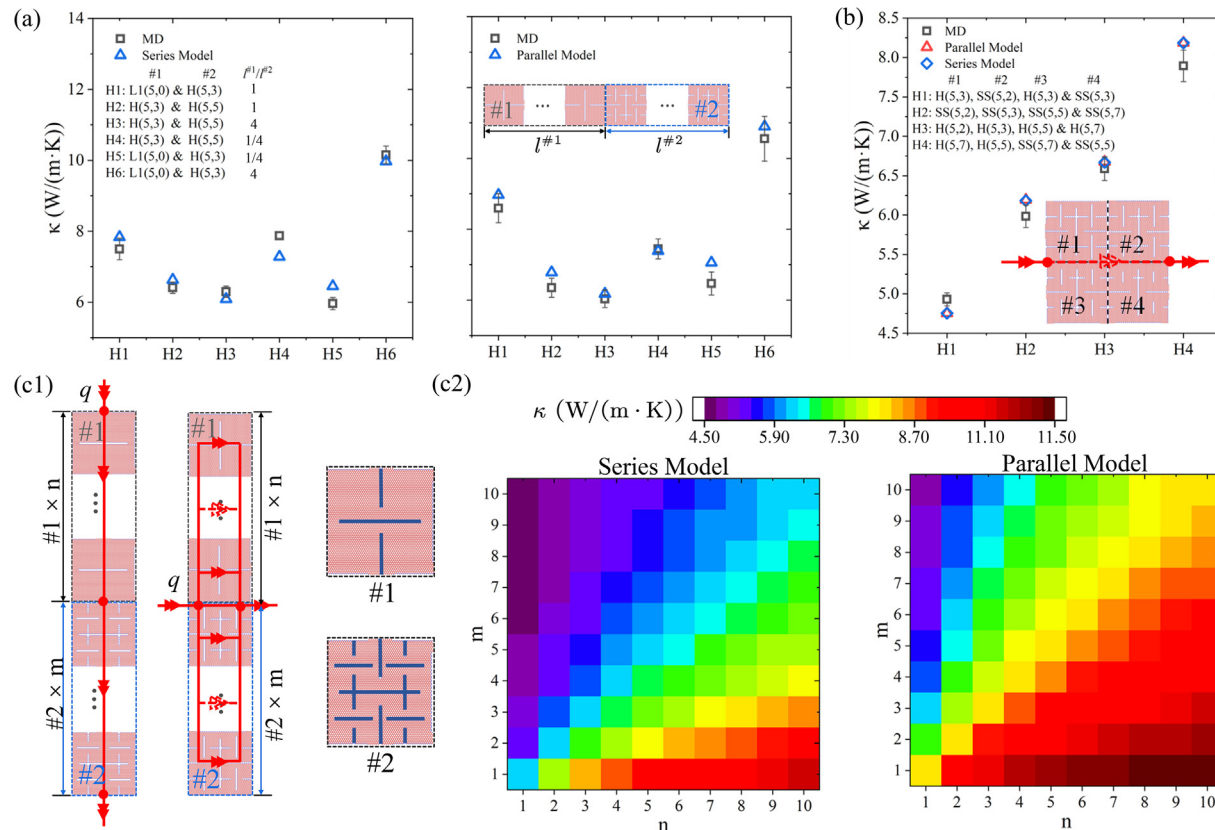


Fig. 6. (a) Thermal conductivity of homogeneous GS-k is predicted by analytical models and MD; the “level-1”, “hybrid” and “self-similar” are named as “L1”, “H”, and “SS”. The building blocks are presented as $L1(i,0)$, $H(i,j)$, and $SS(i,j)$; i and j represent the hinge widths that are $i \times a_0$ (level-1 cut) and $j \times a_0$ (level-2 cut), where $a_0 = 0.246$ nm is a lattice constant of graphene [45]. (b) Thermal conductivity of the heterogeneous GS-k comprising four different hierarchical level-2 building blocks as predicted by two analytical models and MD. (c1) Schematic of heterogeneous GS-k; (c2) the thermal conductivity of heterogeneous GS-k systems composed by level-1 ($m_1/l = 0.1925$) and level-2 building blocks ($m_1/l = 0.1925$, $m_2/l = 0.077$) characterized by different length ratios as predicted by theoretical models.

assembly of building blocks. Three different arrangements of build blocks are considered to investigate the programmability of the thermal conductivity of GS-k (Fig. 6). We find that the arrangements of building blocks for predicting thermal transport are not as strict as the programming of associated stress-strain responses. Namely, the arrangements are not restricted to similar stress-strain behavior and deformation modes of building blocks. However, the hinges of adjacent building blocks should be connected to guarantee the effective heat transfer between the neighboring building blocks, i.e., the hinge widths of the adjacent building blocks are required to be identical. Supposing two combined heterogeneous kirigami nanostructures that comprise n unit cells in series and parallel, respectively, the thermal conductivity (κ) of the combined system can be driven as (see [Supplementary Material S17](#) for more details):

$$\kappa_s = \frac{n}{\sum_{i=1}^{i=n} \frac{1}{\kappa_i}} \text{ (in - series)} \quad (8)$$

$$\kappa_p = \frac{\sum_{i=1}^{i=n} \kappa_i}{n} \text{ (in - parallel)} \quad (9)$$

where κ_i is the thermal conductivity of i^{th} building block.

To verify the analytical models, the predictions and MD results of heterogeneous GS-k are plotted in Fig. 6a. The figures demon-

strate a good agreement between the two results indicating that the theoretical models can be employed to analyze the heat transfer behavior and engineer GS-k to achieve targeted thermal conductivity by altering geometrical and hierarchical features. The ratio of the length, $l^{\#1}/l^{\#2}$, is also considered to further tune the heat transfer of the heterogeneous system in Fig. 6a. We also consider a more complex combination in Fig. 6b. The system is composed of four hierarchical level-2 GS-k unit cells characterized by different hierarchical hinge widths (m_2) and cutting patterns. Based on the abovementioned analytical theory, two different analytical models are constructed to determine the thermal conductivity of the system (See S17 in [Supplementary Material](#) for more details). As shown in Fig. 6b, both theoretical models exhibit a good agreement with MD results for combined systems. Next, we select level-1 ($m_1/l = 0.1925$) and Hybrid Level-2 ($m_1/l = 0.1925$, $m_2/l = 0.077$) as building blocks to explore the tunability and programmability of thermal conductivity by creating the heterogeneous systems (Fig. 6c1). Data shown in Fig. 6c2 are obtained based on our theoretical models. Generally, the developed analytical models offer a tool for the rapid engineering of thermal conductivity of GS-k.

After investigating the programmable mechanical and thermal properties, we also explore the possibility of arranging the building blocks to reveal the information in the form of an image induced by local out-of-plane buckling when subjected to a tensile load. The

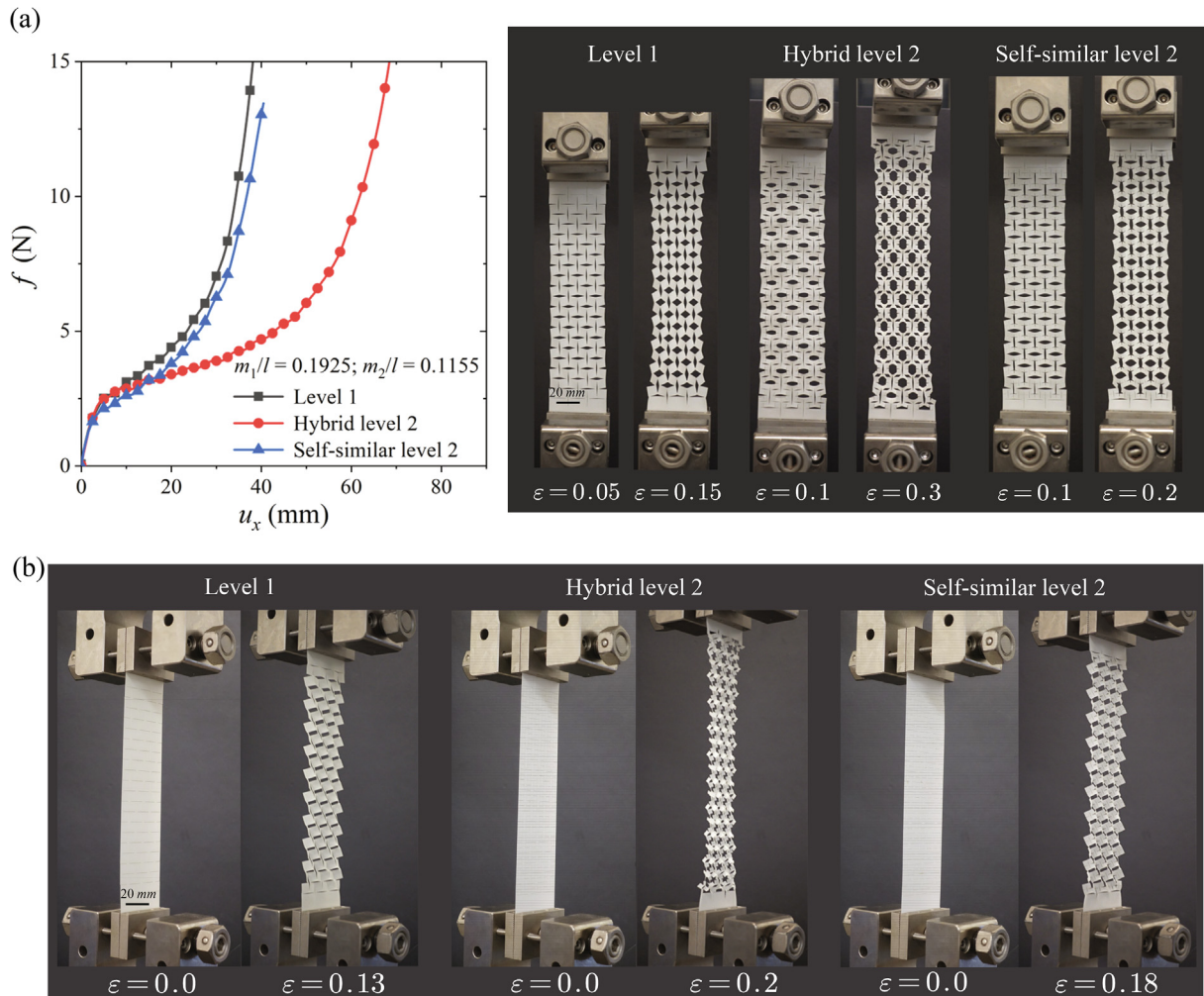


Fig. 7. (a) Mechanical response of kirigami sheets comprising 3×10 unit cells subjected to a quasi-static uniaxial tension. The dimension of each unit cell is $18.33 \text{ mm} \times 18.33 \text{ mm}$. (b) Uniform out-of-plane deformation of kirigami sheets subjected to tensile load.

result of programming surface texture is presented in [Supplementary Material S18](#).

9. Experiments

After conducting the multiscale simulations of GS-k, we first manufacture the kirigami structures out of the graphene sheets ([S19](#) in [Supplementary Material](#)). However, the hinges are not strong enough to support the opening of the kirigami cuts ([Movie S3](#)). To further explore the deformation process and the induced 3D patterns in experiments, kirigami specimens are fabricated out of plastic sheets (Trotec, LaserFlex) by laser cutting (Trotec, Speedy 100) in the form of an array of 3×10 orthogonal cuts ([Fig. 7a](#)). The response of the fabricated kirigami structures is characterized by using a uniaxial tensile test machine (ADMET, eXpert 8612), and their deformations are recorded using a digital camera (Sony RX100IV). In the experiment, the kirigami sheets show similar stress-strain response and out-of-plane deformation-induced 3D patterns as observed in multiscale simulations when subjected to a uniaxial tension load ([Fig. 7b](#)). To validate the FE simulation, we have compared the experimental and FE results of the level-1 kirigami sheet ($m_1/l = 0.1925$) under a uniaxial tension. As shown in [Fig. S23](#) in [Supplementary Material](#), the force-displacement response and deformation mode show excellent agreement between FE and experimental results. Quasi-static uniaxial test results on fabricated kirigami sheets are presented in [Supplementary Material S20](#).

10. Concluding remarks

In summary, we investigate the tunable and programmable thermo-mechanical properties of kirigami-inspired graphene and CNT metamaterials. Our results show that the stress-strain response can be tuned, and the different buckling-induced 3D patterns can be triggered by altering the geometrical parameters as well as the hierarchy of cutting patterns. The thermal conductivity of GS-k and CNT-k decreases monotonically with the decreased hinge width and the increased architectural hierarchical level. The thermal conductivity can be further tuned by external tensile strain. The multiscale simulations (MD and FE) are conducted to illustrate the scale effect. The effective stiffness of GS-k in the initial linear elastic region shows the great deviation between nano-(*MD results*) and microscale (*FE and theoretical results*) owing to the size effect in nanoscale, the curved surface after equilibrium, and the overestimated thickness in nanoscale. Besides, the nano GS-k shows a distinct plastic deformation characterized by zigzag-like curves compared with the kirigami samples in micro/mesoscale due to the specific bond-connected nanostructure. The phonon scattering contributes to the decrease of thermal conductivity in nanoscale, while the effect of phonon scattering on the suppression of thermal transport vanishes in microscale, leading to the deviation of thermal conductivity in different length scales. Furthermore, we find that the stress-strain response, thermal conductivity, as well as buckling-induced 3D patterns can be programmed by combining alternative kirigami building blocks with different geometrical parameters, cutting patterns, and connections (in series/parallel). The established theoretical models can effectively predict and program the stress-strain response and thermal conductivity of combined heterogeneous GS-k. Generally, our closed-form theoretical models offer an efficient way to design the nano-architected metamaterials with desired thermo-mechanical properties. These findings are expected to facilitate the understanding and applications of programmable kirigami-inspired nano-metamaterials and provide thermal management solutions. Our work opens avenues for the next-generation wear-

able nanoelectronics, surface-functionalized nanodevices, and nanoscale heat transport systems.

Declaration of Competing Interest

None.

Acknowledgements

This research was undertaken, in part, thanks to funding from the Canada Research Chairs program to A.H.Akbarzadeh in Multi-functional Metamaterials. A.H. Akbarzadeh also acknowledges the financial supports by Natural Sciences and Engineering Research Council of Canada through NSERC Discovery Grant (RGPIN-2016-0471) and Canada Foundation for Innovation (CFI) through John R. Evans Leaders Fund. J. Cai acknowledges the financial support provided by the China Scholarship Council [File No. 201909370077] and McGill University. The authors acknowledge the assists of Didier Duque (Trotec Laser Canada Inc.) for cutting graphene sheets and discussion with Armin Mirabolghasemi (AM³L lab at McGill University) on thermal properties of architected metamaterials.

Appendix A. Supplementary data

Supplementary data to this article can be found online at <https://doi.org/10.1016/j.matdes.2021.109811>.

References

- [1] A.H. Castro Neto, F. Guinea, N.M.R. Peres, K.S. Novoselov, A.K. Geim, The electronic properties of graphene, *Rev. Mod. Phys.* 81 (1) (2009) 109–162.
- [2] C. Lee, X. Wei, J.W. Kysar, J. Hone, Measurement of the elastic properties and intrinsic strength of monolayer graphene, *Science* 321 (5887) (2008) 385–388.
- [3] A.A. Balandin, Thermal properties of graphene and nanostructured carbon materials, *Nat Mater* 10 (8) (2011) 569–581.
- [4] A.H. Castro Neto, The carbon new age, *Mater. Today* 13 (3) (2010) 12–17.
- [5] P. Zhang, L. Ma, F. Fan, Z. Zeng, C. Peng, P.E. Loya, Z. Liu, Y. Gong, J. Zhang, X. Zhang, P.M. Ajayan, T. Zhu, J. Lou, Fracture toughness of graphene, *Nat Commun* 5 (2014) 3782.
- [6] S. Hong, H. Lee, J. Lee, J. Kwon, S. Han, Y.D. Suh, H. Cho, J. Shin, J. Yeo, S.H. Ko, Highly stretchable and transparent metal nanowire heater for wearable electronics applications, *Adv Mater* 27 (32) (2015) 4744–4751.
- [7] A.M. Hussain, F.A. Ghaffar, S.I. Park, J.A. Rogers, A. Shamsim, M.M. Hussain, Metal/Polymer Based Stretchable Antenna for Constant Frequency Far-Field Communication in Wearable Electronics, *Adv. Funct. Mater.* 25 (42) (2015) 6565–6575.
- [8] M.K. Blees, A.W. Barnard, P.A. Rose, S.P. Roberts, K.L. McGill, P.Y. Huang, A.R. Ruyack, J.W. Kevek, B. Kobrin, D.A. Muller, P.L. McEuen, Graphene kirigami, *Nature* 524 (7564) (2015) 204–207.
- [9] N. An, A.G. Domel, J. Zhou, A. Rafsanjani, K. Bertoldi, Programmable Hierarchical Kirigami, *Adv. Funct. Mater.* (2019).
- [10] S.H. Chen, K.C. Chan, D.X. Han, L. Zhao, F.F. Wu, Programmable super elastic kirigami metallic glasses, *Mater. Des.* 169 (2019).
- [11] T. Chen, K. Shea, Computational design of multi-stable, reconfigurable surfaces, *Mater. Des.* (2021).
- [12] C. Song, S. Li, H. Bao, J. Ju, Design of thermal diodes using asymmetric thermal deformation of a Kirigami structure, *Mater. Des.* 193 (2020).
- [13] A. Rafsanjani, K. Bertoldi, Buckling-Induced Kirigami, *Phys Rev Lett* 118 (8) (2017) 084301.
- [14] W. Wu, W. Hu, G. Qian, H. Liao, X. Xu, F. Berto, Mechanical design and multifunctional applications of chiral mechanical metamaterials: A review, *Mater. Des.* 180 (2019).
- [15] L. Yuan, H. Dai, J. Song, J. Ma, Y. Chen, The behavior of a functionally graded origami structure subjected to quasi-static compression, *Mater. Des.* 189 (2020).
- [16] L. Mizzi, E.M. Mahdi, K. Titov, R. Gatt, D. Attard, K.E. Evans, J.N. Grima, J.-C. Tan, Mechanical metamaterials with star-shaped pores exhibiting negative and zero Poisson's ratio, *Mater. Des.* 146 (2018) 28–37.
- [17] X. Zhang, L. Medina, H. Cai, V. Aksyuk, H.D. Espinosa, D. Lopez, Kirigami Engineering-Nanoscale Structures Exhibiting a Range of Controllable 3D Configurations, *Adv Mater* 33 (5) (2021) e2005275.
- [18] J. Feng, W. Li, X. Qian, J. Qi, L. Qi, J. Li, Patterning of graphene, *Nanoscale* 4 (16) (2012) 4883–4899.
- [19] H. Wang, S. Hu, K. Takahashi, X. Zhang, H. Takamatsu, J. Chen, Experimental study of thermal rectification in suspended monolayer graphene, *Nat Commun* 8 (2017) 15843.

- [20] N. Wei, Y. Chen, K. Cai, J. Zhao, H.-Q. Wang, J.-C. Zheng, Thermal conductivity of graphene kirigami: Ultralow and strain robustness, *Carbon* 104 (2016) 203–213.
- [21] B. Zheng, G.X. Gu, Tuning graphene mechanical anisotropy via defect engineering, *Carbon* (2019).
- [22] A. Rafsanjani, L. Jin, B. Deng, K. Bertoldi, Propagation of pop ups in kirigami shells, *Proc Natl Acad Sci U S A* 116 (17) (2019) 8200–8205.
- [23] Y. Tang, G. Lin, S. Yang, Y.K. Yi, R.D. Kamien, J. Yin, Programmable Kiri-Kirigami Metamaterials, *Adv Mater* 29 (10) (2017).
- [24] Y. Tang, Y. Li, Y. Hong, S. Yang, J. Yin, Programmable active kirigami metasheets with more freedom of actuation, *Proc Natl Acad Sci U S A* (2019).
- [25] L. Jin, A.E. Forte, B. Deng, A. Rafsanjani, K. Bertoldi, Kirigami-Inspired Inflatables with Programmable Shapes, *Adv Mater* 32 (33) (2020) e2001863.
- [26] S.J.P. Callens, A.A. Zadpoor, From flat sheets to curved geometries: Origami and kirigami approaches, *Mater. Today* 21 (3) (2018) 241–264.
- [27] B. Mortazavi, A. Lherbier, Z. Fan, A. Harju, T. Rabczuk, J.C. Charlier, Thermal and electronic transport characteristics of highly stretchable graphene kirigami, *Nanoscale* 9 (42) (2017) 16329–16341.
- [28] Y. Gao, B. Xu, van der Waals Graphene Kirigami Heterostructure for Strain-Controlled Thermal Transparency, *ACS Nano* 12 (11) (2018) 11254–11262.
- [29] K.S. Novoselov, V.I. Fal'ko, L. Colombo, P.R. Gellert, M.G. Schwab, K. Kim, A roadmap for graphene, *Nature* 490 (7419) (2012) 192–200.
- [30] H. Chen, X.L. Zhang, Y.Y. Zhang, D. Wang, D.L. Bao, Y. Que, W. Xiao, S. Du, M. Ouyang, S.T. Pantelides, H.J. Gao, Atomically precise, custom-design origami graphene nanostructures, *Science* 365 (6457) (2019) 1036–1040.
- [31] S. Plimpton, Fast Parallel Algorithms for Short-Range Molecular Dynamics, *J. Comput. Phys.* 117 (1) (1995) 1–19.
- [32] A. Stukowski, Visualization and analysis of atomistic simulation data with OVITO—the Open Visualization Tool, *Modell. Simul. Mater. Sci. Eng.* 18 (1) (2010).
- [33] F. Müller-Plathe, A simple nonequilibrium molecular dynamics method for calculating the thermal conductivity, *J. Chem. Phys.* 106 (14) (1997) 6082–6085.
- [34] H. Ghasemi, A. Rajabpour, A.H. Akbarzadeh, Tuning thermal conductivity of porous graphene by pore topology engineering: Comparison of non-equilibrium molecular dynamics and finite element study, *Int. J. Heat Mass Transf.* 123 (2018) 261–271.
- [35] J.-X. Shi, T. Natsuki, X.-W. Lei, Q.-Q. Ni, Equivalent Young's modulus and thickness of graphene sheets for the continuum mechanical models, *Appl. Phys. Lett.* 104 (22) (2014).
- [36] S. Zhu, T. Li, Hydrogenation-assisted graphene origami and its application in programmable molecular mass uptake, storage, and release, *ACS Nano* 8 (3) (2014) 2864–2872.
- [37] Y. Cho, J.H. Shin, A. Costa, T.A. Kim, V. Kunin, J. Li, S.Y. Lee, S. Yang, H.N. Han, I.S. Choi, D.J. Srolovitz, Engineering the shape and structure of materials by fractal cut, *Proc Natl Acad Sci U S A* 111 (49) (2014) 17390–17395.
- [38] Y. Gao, W. Yang, B. Xu, Unusual thermal conductivity behavior of serpentine graphene nanoribbons under tensile strain, *Carbon* 96 (2016) 513–521.
- [39] T. Wassmann, A.P. Seitsonen, A.M. Saitta, M. Lazzari, F. Mauri, Structure, stability, edge states, and aromaticity of graphene ribbons, *Phys Rev Lett* 101 (9) (2008) 096402.
- [40] C. Zhang, A. Akbarzadeh, W. Kang, J. Wang, A. Mirabolghasemi, Nano-architected metamaterials: Carbon nanotube-based nanotresses, *Carbon* 131 (2018) 38–46.
- [41] J. Hone, M. Whitney, A. Zettl, Thermal conductivity of single-walled carbon nanotubes, *Synth. Met.* 103 (1–3) (1999) 2498–2499.
- [42] S. Babaee, S. Pajovic, A. Rafsanjani, Y. Shi, K. Bertoldi, G. Traverso, Bioinspired kirigami metasurfaces as assistive shoe grips, *Nat. Biomed Eng* (2020).
- [43] S. Bazrafshan, A. Rajabpour, Engineering of thermal transport in graphene using grain size, strain, nitrogen and boron doping: a multiscale modeling, *Int. J. Heat Mass Transf.* 123 (2018) 534–543.
- [44] T. van Manen, S. Janbaz, M. Ganjian, A.A. Zadpoor, Kirigami-enabled self-folding origami, *Mater. Today* 32 (2020) 59–67.
- [45] C. Chen, J. Avila, H. Arezki, V.L. Nguyen, J. Shen, M. Mucha-Kruczynski, F. Yao, M. Bouthchich, Y. Chen, Y.H. Lee, M.C. Asensio, Large local lattice expansion in graphene adlayers grown on copper, *Nat Mater* 17 (5) (2018) 450–455.